ADVANCED THEORY AND SIMULATIONS
www.advtheorysimul.com

Revisiting the Dielectric Breakdown in a Polycrystalline Ferroelectric: A Phase-Field Simulation Study

Mohammad Khondabi, Hossein Ahmadvand, and Mahdi Javanbakht*

To understand the dielectric breakdown in a polycrystalline ferroelectric, a thorough phase field simulation has been performed by introducing a new degradation function. Time and position evolution of breakdown path, electric field dependence of breakdown time, and the effect of several parameters such as grain orientation, dielectric constant of grain and grain-boundaries (GBs), thickness of GBs (d_{GB}), and grain size (G_a) on the threshold breakdown electric field, E_{BT}, are investigated. The results indicate that E_{BT} is improved with decreasing dielectric constant. The dependence of E_{BT} on grain size and GB's thickness obeys a power function G_a^{-n} ($n = 0.42$) and d_{GB}^{n} ($n = 0.3$), respectively. The results help to engineer the grains and GBs properties and achieve a high breakdown electric field, which is very important in energy-storage applications.

1. Introduction

Nowadays, electrical energy storage is vital for green and renewable energy applications. Dielectric capacitors exhibit higher charge/discharge rate than batteries, which makes them suitable for pulse power systems.[1–3] Pulse power technology has been widely used in many fields, such as systems including electric gun, high-power laser, plasma generation, and so on.[4–8] If the energy density of the dielectric capacitors can be improved to be competitive with electrochemical capacitors or even batteries, their application range will be extended.[9] Upon an applied electric field, the energy density (U_e) of a dielectric can be calculated from the integral of product of the electric field (E) and the electric displacement (D) that is, $\int_0^D E\mathrm{d}D$. In linear approximation, the maximal energy density can be expressed by $1/2\varepsilon_0\varepsilon_r E_{BT}^2$, where ε_0 is the vacuum permittivity, ε_r is the relative dielectric permittivity, and E_{BT} is the threshold breakdown electric field. Therefore, U_e depends on ε_r and E_{BT}, and thus, increasing E_{BT} is an effective method to achieve high energy density in dielectric capacitors. E_{BT} depends on many factors, such as grain size, impurity, porosity, band gap, thickness, and even sample geometry.[9] A dielectric material usually exhibits an irreversible damage after breakdown, often in the form of a fine tubular conductive channel. The major part of the dielectric material outside the channel remains intact.

The phase field model has emerged as a powerful tool for numerical prediction of evolution processes in materials. It has been successfully applied to simulate the evolution of microstructures with complex morphologies in a wide variety of material processes such as, grain growth,[10–15] martensitic transformation,[16–21] solidification,[22–28] crack propagation problems,[29–34] ferrofluids,[35] and so on. The significant characteristic of phase-field methods is the diffuseness of the interface between two phases. An internal variable, so-called order parameter is defined in such a way that it varies continuously over a thin interfacial layer and is mostly uniform in the bulk phases. This parameter helps us to avoid the tracking of interfaces. The time rate of change of this variable in relation with energy minimization can be used to investigate the dielectric breakdown in ferroelectrics.

Recently, a large number of experimental works have been carried out to improve the threshold breakdown electric field, E_{BT}, and consequently enhancing the energy storage in dielectric materials.[36–46] In particular, Qiao et al. have reported that doping of $Bi_{0.5}Na_{0.5}TiO_3$ with $Sr_{0.7}La_{0.2}TiO_3$ (BNT-SLT solid solution) has reduced the grain size, increased band gap, and reduced the tolerance factor, which results in a threshold breakdown electric field, E_{BT}, of 315 kV cm^{-1}.[36] It has been reported that doping of $BiFeO_3$-$BaTiO_3$ with $NaNbO_3$, significantly enhanced E_{BT} to about 360 kV cm^{-1}, which is attributed to enhanced band gap, decreased grain size, and increased resistivity.[41] Li et al. have used a two-step strategy, including doping of Nd^{3+} to modify the microstructure and use of viscous polymer processing route, to prepare $(Ba_{0.65}Sr_{0.245}Bi_{0.07})_{0.99}Nd_{0.01}TiO_3$ compound. This strategy significantly increased the density of the samples and reduced the cavities, as a result of which E_{BT} was greatly improved to 460 kV cm^{-1}.[46] Despite several experimental works, the role of different parameters on E_{BT} is not fully understood. On the other side, there are very few computational works based on phase field model to study the dielectric breakdown and energy storage in ferroelectric ceramic materials.[47–50] Thus, further and in-depth investigation is required to understand the nature of dielectric

M. Khondabi, H. Ahmadvand
Department of Physics
Isfahan University of Technology
Isfahan 84156-83111, Iran
E-mail: ahmadvand@iut.ac.ir
M. Javanbakht
Department of Mechanical Engineering
Isfahan University of Technology
Isfahan 84156-83111, Iran

The ORCID identification number(s) for the author(s) of this article can be found under https://doi.org/10.1002/adts.202200314

DOI: 10.1002/adts.202200314

breakdown in ferroelectric materials. In this work we report on a thorough study on the dielectric breakdown, its time and position evolution, E-field dependence of breakdown time, role of dielectric constant of grain and grain boundaries (GB), and the effect of grain-size and GBs thickness on the threshold breakdown electric field, E_{BT}.

2. Simulation Processing Details

2.1. Dielectric Constant of a Ferroelectric

According to LGD theory, considering the perovskite-type structure in the paraelectric state, and assuming that this structure could be treated as a strained cubic crystal, the free energy for a ferroelectric can be written as[51]

$$F(P,T) = F(0,T) + \frac{\alpha}{2}P^2 + \frac{\beta}{4}P^4 + \frac{\gamma}{6}P^6 + \cdots \quad (1)$$

where α is a temperature-dependent coefficient, P is polarization, and β and γ are temperature-independent coefficients. Above the Curie temperature in the paraelectric state, α can be written as follows[52]

$$\alpha = C(T - T_C) = \frac{1}{\varepsilon(0)} = \frac{1}{\varepsilon_0 \varepsilon_r(0)} \quad (2)$$

where C is a constant, T_C is the Curie–Weiss temperature, $\varepsilon(0)$ is the dielectric permittivity at zero E-field, ε_0 is the permittivity of space, and $\varepsilon_r(0)$ is the relative dielectric permittivity at zero E-field. From Equation (1), we have

$$\frac{\partial F}{\partial P} = E = \alpha P + \beta P^3 + \gamma P^5 + \cdots \quad (3)$$

and then we can obtain

$$\frac{\partial E}{\partial P} \approx \frac{1}{\varepsilon_0 \varepsilon_r} = \frac{1}{\varepsilon_0 \varepsilon_r(0)} P + 3\beta P^2 + 5\gamma P^4 + \cdots \quad (4)$$

In the case of small fields, we can neglect terms in P^4 or greater. Also, for $\varepsilon \gg 1$, polarization is related to the electric field as follows

$$P = \varepsilon_0 \varepsilon_r(E) E \quad (5)$$

By replacing P from Equation (5) into Equation (4), we can obtain

$$\frac{1}{\varepsilon_0 \varepsilon_r} = \frac{1}{\varepsilon_0 \varepsilon_r(0)} + 3\beta(\varepsilon_0 \varepsilon_r)^2 E^2 \quad (6)$$

which can be rewritten as follows

$$\frac{\varepsilon_r}{\varepsilon_r(0)} = \frac{\left[1 - \frac{\varepsilon_r}{\varepsilon_r(0)} + \left(\frac{\varepsilon_r}{\varepsilon_r(0)}\right)^3\right]^{1/3}}{\left[1 + 3\beta\left(\varepsilon_0 \varepsilon_r(0)\right)^3 E^2\right]^{1/3}} \quad (7)$$

The value of the numerator is always around 1, thus, Equation (7) becomes simply

$$\varepsilon_r(E) = \frac{\varepsilon_r(0)}{(1 + \lambda E^2)^{1/3}} \quad (8)$$

Table 1. The parameters used in the simulations..

Parameter	Value	Definition
L	1000nm	Length of model
H	2000nm	Height of model
G_a	450nm	Average grain size
d_{GB}	20nm	Grain boundary thickness
h	1nm	Mesh size
β	$3 \times 10^{10} Vm^3C^{-3}$	LGD parameter
ε_0	$8.854 \times 10^{-12} CV^{-1}m^{-1}$	Permittivity of space
$\varepsilon_G(0)$	1000	The relative dielectric permittivity of the grain at zero electric field
ε_{GB}	100	The relative dielectric permittivity of the grain boundary
δ	30nm	Length scale to regularize damaged-intact interface
Γ_G	$5 \times 10^{-10} Jm^{-1}$	Constant coefficient related to the breakdown energy of the grain
Γ_{GB}	$5 \times 10^{-9} Jm^{-1}$	Constant coefficient related to the breakdown energy of the grain boundary
m	$0.1 m^3 J^{-1} s^{-1}$	Mobility parameter related to speed of the breakdown propagation
μ	10^{-3}	A small positive constant meant to numerical stability

where $\lambda = 3\beta(\varepsilon_0 \varepsilon_r(0))^3$. β is given in **Table 1**. Equation (8) is known as Johnson's relationship.[51]

Figure 1 shows the relative dielectric permittivity as a function of DC electric field using Equations (7) and (8) (Johnson's relation) for a typical ferroelectric. The maximum difference between the two curves is about 19% which is seen at lower E-fields. This difference is small in high electric fields. Thus, Johnson's analytical equation has been used to reduce the computational cost.

2.2. Phase-Field Model for Dielectric Breakdown

In a standard phase field model, a continuous phase-field variable $\eta(\vec{r}, t)$ is introduced to characterize the electrostatic damage state in the dielectric material, where $\vec{r}$ is position vector and t is time. At positions where the material is in the complete damaged state, η is 0, while in the intact positions, the value of phase-field variable η equals to 1. The fully damaged state becomes conductive. Mathematically, it can be modeled as a dielectric material with very high permittivity. For this purpose, we consider the permittivity as a function of the phase-field variable, η, as follows[47]

$$\varepsilon(\eta) = \frac{\varepsilon_{ini}}{g(\eta) + \mu} \quad (9)$$

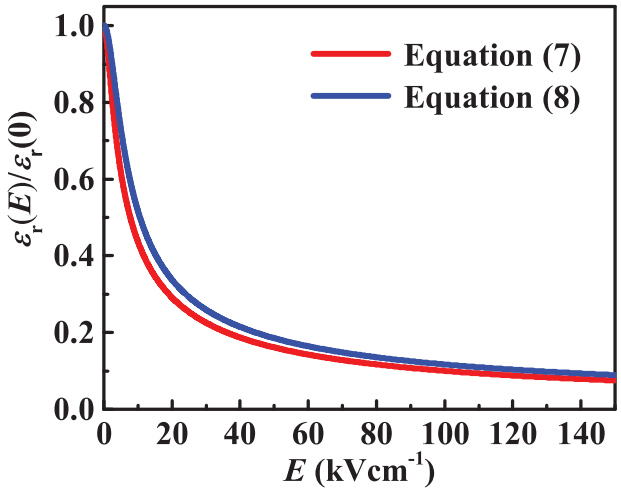

Figure 1. The DC electric field dependence of the relative dielectric permittivity using Equations (7) and (8) (Johnson's relation) for a typical ferroelectric.

where ε_{ini} is the initial permittivity, $g(\eta)$ is the degradation function, which is a crucial part to describe the propagation of a tubular conductive channel in the phase-field model. A proper choice of the degradation function $g(\eta)$ will be discussed in following. μ is a small positive constant meant to numerical stability where $g(\eta) = 0$, which was first used by Ambrosio and Tortorelli.[53] In the current study, we set $\mu = 10^{-3}$.[47]

The polycrystalline ferroelectric materials consist of grains and GBs. The relative permittivity of grains is dependent on electric field (Equation (8)), while the relative permittivity of the GB is taken to be field independent. Thus

$$\varepsilon_{ini}(\vec{\nabla}\phi) = \begin{cases} \frac{\varepsilon_G(0)}{(1+\lambda\vec{\nabla}\phi\cdot\vec{\nabla}\phi)^{1/3}} & \text{in grain} \\ \varepsilon_{GB} & \text{onGB} \end{cases} \tag{10}$$

The total free energy per unit volume of the switched process can be written as

$$U(\vec{\nabla}\phi, \eta, \vec{\nabla}\eta) = U_{es}(\vec{\nabla}\phi, \eta) + U_d(\eta) + U_i(\vec{\nabla}\eta) \tag{11}$$

where $U_{es}(\vec{\nabla}\phi, \eta)$ is the electrostatic energy, $U_d(\eta)$ is the energy of damage, and $U_i(\vec{\nabla}\eta)$ is the gradient energy, which take the following forms[47]

$$U_{es}(\vec{\nabla}\phi, \eta) = \begin{cases} -\int_0^{E_{max}} \frac{\varepsilon_0\varepsilon_G(\eta)E}{(1+\lambda\vec{\nabla}\phi\cdot\vec{\nabla}\phi)^{1/3}} dE & \text{in grain} \\ -\frac{\varepsilon_0\varepsilon_{GB}(\eta)}{2}\vec{\nabla}\phi\cdot\vec{\nabla}\phi & \text{onGB} \end{cases} \tag{12}$$

$$U_d(\eta) = \frac{\Gamma}{\delta^2}[1 - g(\eta)] \tag{13}$$

$$U_i(\vec{\nabla}\eta) = \frac{\Gamma}{4}\vec{\nabla}\eta\cdot\vec{\nabla}\eta \tag{14}$$

In Equation (13), Γ is related to the breakdown energy. The parameter δ has the dimension of length and is often referred to as regularization length, since it controls the width of the transition zone of the phase field order parameter between the intact state, $\eta = 1$, and the damaged state, $\eta = 0$. Γ/δ^2 is the critical energy density to initiate local damage. $U_i(\vec{\nabla}\eta)$ characterizes the diffuse interface between the intact and damaged phases. The total free energy of the ferroelectric material can be obtained by integrating U over the grains and GBs, as follows

$$F_G(\eta, \phi) = \int_\Omega \left[-\int_0^{E_{max}} \frac{\varepsilon_0\varepsilon_G(\eta)E}{(1+\lambda\vec{\nabla}\phi\cdot\vec{\nabla}\phi)^{1/3}} dE + \frac{\Gamma_G}{\delta^2}[1 - g(\eta)] + \frac{\Gamma_G}{4}\vec{\nabla}\eta\cdot\vec{\nabla}\eta \right] dV \tag{15}$$

$$F_{GB}(\eta, \phi) = \int_\Omega \left[-\frac{\varepsilon_0\varepsilon_{GB}(\eta)}{2}\vec{\nabla}\phi\cdot\vec{\nabla}\phi + \frac{\Gamma_{GB}}{\delta^2}[1 - g(\eta)] + \frac{\Gamma_{GB}}{4}\vec{\nabla}\eta\cdot\vec{\nabla}\eta \right] dV \tag{16}$$

The evolution of the η and ϕ are controlled by the variation of the total free energy, F,

$$\frac{\delta F}{\delta\phi} = 0 \tag{17}$$

$$\frac{\delta F}{\delta\eta} = -\frac{1}{m}\frac{\partial\eta}{\partial t} \tag{18}$$

where m is the mobility parameter that controls the speed of the breakdown propagation in ferroelectric materials. Equation (17) can be rewritten as follows

$$-\vec{\nabla}\cdot\left(\frac{\partial U(\vec{\nabla}\phi, \eta, \vec{\nabla}\eta)}{\partial\vec{\nabla}\phi}\right) + \frac{\partial U(\vec{\nabla}\phi, \eta, \vec{\nabla}\eta)}{\partial\phi} = 0 \tag{19}$$

The second term in Equation (19) is zero, because U is not implicitly dependent on ϕ. Thus

$$\vec{\nabla}\cdot\left(\frac{\partial U(\vec{\nabla}\phi, \eta, \vec{\nabla}\eta)}{\partial\vec{\nabla}\phi}\right) = 0 \tag{20}$$

By replacing the term inside the integral of Equations (15) and (16) in Equation (20), the equilibrium equations, for the grains and GBs, are obtained as

$$\vec{\nabla}\cdot\left[\varepsilon_G(\eta)\left(1 + \lambda\vec{\nabla}\phi\cdot\vec{\nabla}\phi\right)^{-1/3}\vec{\nabla}\phi\right] = 0 \tag{21}$$

$$\vec{\nabla}\cdot\left[\varepsilon_{GB}(\eta)\vec{\nabla}\phi\right] = 0 \tag{22}$$

Equation (18) can be rewritten as follows

$$-\vec{\nabla}\cdot\left(\frac{\partial U(\vec{\nabla}\phi, \eta, \vec{\nabla}\eta)}{\partial\vec{\nabla}\eta}\right) + \frac{\partial U(\vec{\nabla}\phi, \eta, \vec{\nabla}\eta)}{\partial\eta} = -\frac{1}{m}\frac{\partial\eta}{\partial t} \tag{23}$$

By replacing the term inside the integral of Equations (15) and (16) in Equation (23) the time-dependent Ginzburg–Landau

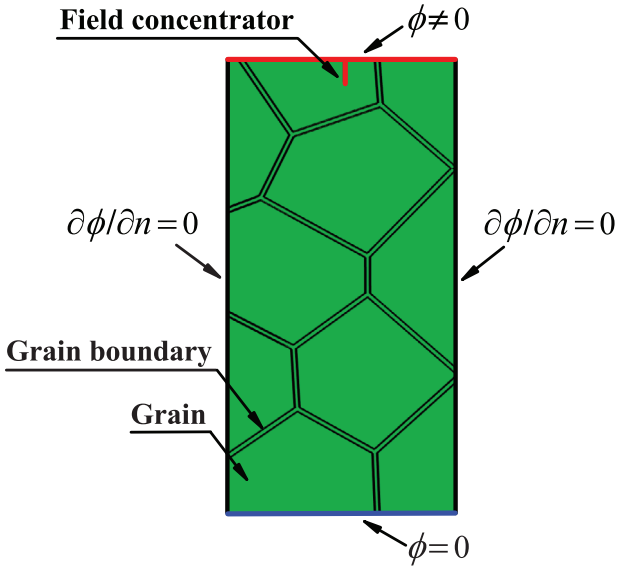

Figure 2. Geometry and boundary conditions of the 2D phase-field model, containing grains and GBs, with a thin conductive field concentrator connected to the top electrode.

equations, for the grains and GBs, can be obtained as

$$\frac{1}{m}\frac{\partial \eta}{\partial t} = \frac{3\varepsilon_0 \varepsilon'_G(\eta)}{4\lambda}\left[\left(1+\lambda\vec{\nabla}\phi\cdot\vec{\nabla}\phi\right)^{2/3}-1\right]+\frac{\Gamma_G}{\delta^2}g'(\eta)+\frac{\Gamma_G}{2}\vec{\nabla}^2\eta \tag{24}$$

$$\frac{1}{m}\frac{\partial \eta}{\partial t} = \frac{\varepsilon_0 \varepsilon'_{GB}(\eta)}{2}\vec{\nabla}\phi\cdot\vec{\nabla}\phi+\frac{\Gamma_{GB}}{\delta^2}g'(\eta)+\frac{\Gamma_{GB}}{2}\vec{\nabla}^2\eta \tag{25}$$

2.3. Modeling

The COMSOL Multiphysics is used to solve the coupled Equations (21), (22), (24), and (25). These equations are solved using the heat equation solver, which is available in the classical PDEs module. The governing equations are solved with finite element (FE) method. For discretization of the geometry a fine enough mesh size (1 nm) is used for triangular Lagrange elements. In the simulations, the time step is set to 1 μs. However, the adjustable time step option is used, which allows the code to select appropriate time steps to prevent divergence and to reduce the time solution. From the fully coupled and segregated approaches, the fully coupled option was selected to solve the system of nonlinear equations. In the segregated solver, the problem is subdivided into two or more segregated steps, which are solved consecutively within a single iteration, and thus less memory is occupied. In contrast, the fully coupled solver forms a large system of coupled equations that solve for all of the unknowns simultaneously. Thus, it takes up more memory, but gives a more accurate result of the problem.

The material parameters used in the simulations are given in Table 1. The model of ferroelectric ceramic, consisting grains and GBs, is built via Voronoi tessellation. **Figure 2** shows the geometry and boundary conditions of the 2D phase-field model. The length (L) and height (H) of the model are fixed at 1000 and 2000 nm, respectively. The average grain size (G_a) and the GB thickness (d_{GB}) are chosen to be 450 and 20 nm, respectively. To control the initial breakdown, a thin conductive wire is defined as a field concentrator and connected to the top electrode.[47] The value of the phase-field variable η is fixed to be 0 on the field concentrator.

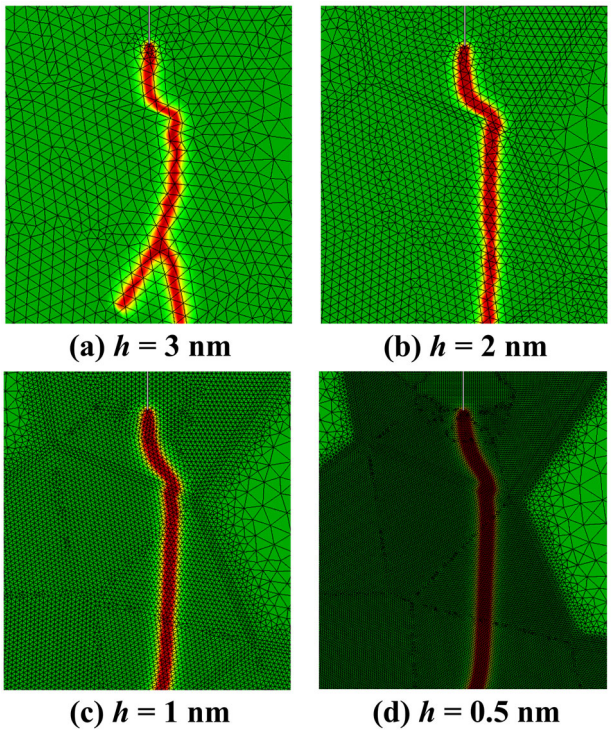

Figure 3. Mesh patterns of a part of the 2D model. The nucleation area is highly meshed as a size of a) h = 3 nm, b) h = 2 nm, c) h = 1 nm, and d) h = 0.5 nm.

Figure 3 shows the mesh patterns of the 2D model. Near the tubular conductive channel path, the mesh size (h) is set to be 3, 2, 1, and 0.5 nm for Figure 3a–d, respectively, and increases as it moves away from the tubular conductive channel path, in order to reduce the computational cost. The propagation path of the channels for Figure 3c,d are similar and smooth. Thus, the mesh size of 1 nm is suitable for discretization of the model.

The degradation function $g(\eta)$ in Equation (9) models the release of electrostatic energy when the phase-field variable η becomes zero. Starting from intact material where $\eta = 1$, the gradient $\vec{\nabla}\eta$ vanishes and the evolution of the phase-field variable mainly depends on the degradation function $g(\eta)$ and the local part of the dielectric breakdown energy. Thus, the choice of this function is highly crucial for modeling dielectric breakdown nucleation. In the published works on ferroelectrics, the authors commonly use the degradation function as follows[47,48]

$$g_1(\eta) = \eta^3(4-3\eta) \tag{26}$$

However, we use the following function for $g(\eta)$,[54] which shows a good convergence.

$$g_2(\eta) = \eta^2(3-2\eta) \tag{27}$$

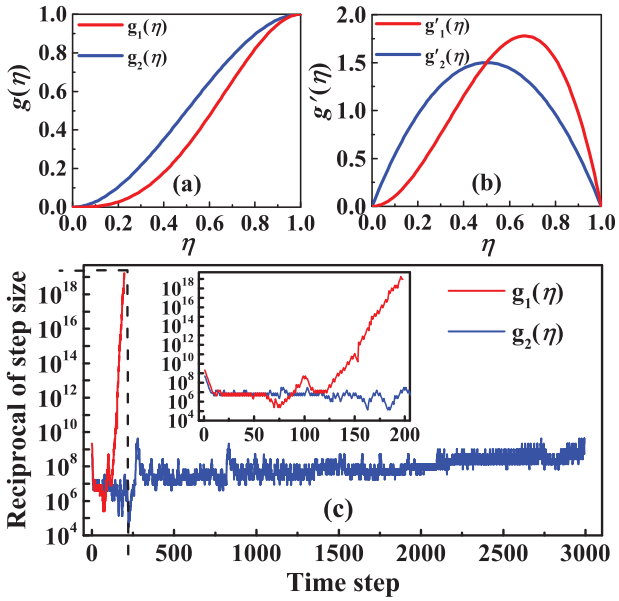

Figure 4. a) Degradation functions $g_1(\eta)$ from Equation (26), and $g_2(\eta)$ from Equation (27), b) derivative of the functions $g_1(\eta)$ and $g_2(\eta)$, and c) reciprocals of step size corresponding to $g_1(\eta)$ and $g_2(\eta)$.

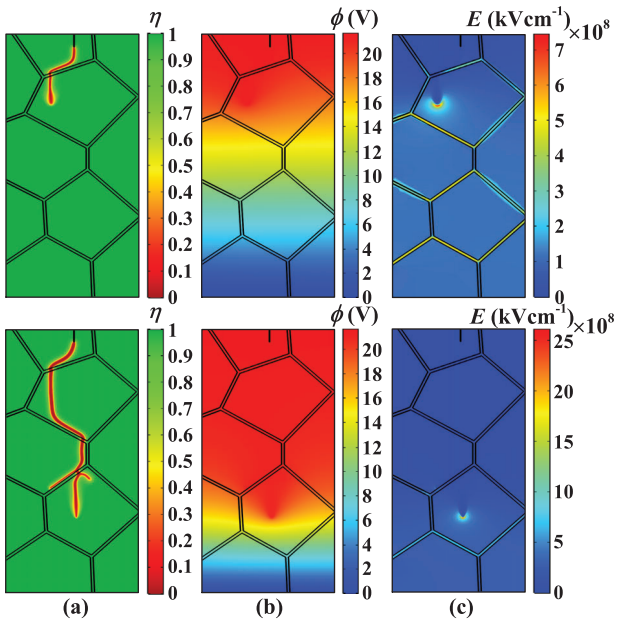

Figure 5. Evolution of the a) phase-field variable, b) local potential, and c) local electric field, at two different times t = 345 μs(top panels) and 415 μs (bottom panels).

For the sake of comparison, the two above degradation functions and their derivatives are plotted in **Figure 4**a,b, respectively. As can be seen, both the functions and their derivatives have the same values at their extrema, i.e., $g_1(0) = g_2(0) = 0$, $g_1(1) = g_2(1) = 1$, $g_1'(0) = g_2'(0) = 0$, and $g_1'(1) = g_2'(1) = 0$. However, $g_2(\eta)$ represents a lower degree polynomial of η which allows for a better numerical convergence. To compare the numerical convergence, the reciprocal of time step size is plotted for a benchmark problem in Figure 4c for both the functions with the same solver settings. It can be seen, the simulation performed using $g_1(\eta)$ diverges while it converges for $g_2(\eta)$. The same happened in almost all the simulations performed. Hence, $g_2(\eta)$ is used in our simulations.

3. Results and Discussions

Figure 5 shows the evolution of the phase-field variable η, local potential ϕ (V), and electric field E (kV cm^{-1}) between the electrodes. The top and bottom figures correspond to the arbitrary times of t = 345 and 415 μs, respectively. The conductive channel begins to propagate at the field concentrator. It propagates through the first grain and then deviates close to the nearest GB. After deviation, the conductive channel continues to propagate through the grain, instead of propagating into the GB. This is because of the higher breakdown energy of the GB relative to the grain.[48,55] If the external electric potential applied between the top and bottom electrodes is not large enough, the conductive channel will not pass across the GB and the breakdown does not occur in the ferroelectric. To reach the threshold breakdown electric potential, we increased the potential by 0.1 V step and repeated the simulation. Finally, in our model, we reached the threshold breakdown at 21.7 V, which is equivalent to an electric field of 108.5 kV cm^{-1}. This value is very well in agreement with experimental results of ferroelectrics.[56,57] Note that, the total width of the channel is in the nanoscale range and is approximately about 70 nm around the middle of the model.

When the conductive channel reaches the lower parts, it's tip becomes sharper and propagates more easily into lower grains and GBs. The reason for this can be found in Figure 5b,c. As shown in Figure 5b, since the conductive channel is connected to the upper edge, as it enters into the lower grains and GBs, makes them equi-potential with the upper electrode. Thus, the value of the local electric field at the tip of the conductive channel increases over time (see Figure 5c), and thus the growth of the conductive channel will be more easy. Here we consider only an initial field concentrator instead of a cavity, defect, impurity, and so on, which usually has less breakdown strength than the base material. However, in real samples there can be a lot of cavities, defects, and impurities, that each of them can contribute to the dielectric breakdown in ferroelectric materials, and destroy the energy storage property. Thus, preparation of dielectric ceramics with minimal cavities, defects, and impurities is one of the most important ways to achieve high dielectric breakdown and excellent energy storage.[58–63]

To see the time evaluation of the breakdown phenomena, the phase-field variable profile at several arbitrary times, t_1 = 10, t_2 = 50, t_3 = 340, t_4 = 375, t_5 = 385, and t_{final} = 420 μs, are depicted in **Figure 6**a–f. Furthermore, Figure 6g shows the time dependence of the total energy, ΔU, with two insets for a better view at the deflection points. When the conductive channel begins to propagate ($t = 0 - 50$μs), the total energy decreases. As discussed above, when the conductive channel reaches the GB, it does not easily propagate into the GB. Interestingly, the total energy remains constant for a large time interval of t = 50–340μs. This corresponds to the robustness of GB against breakdown. When the applied electric field is large enough, the conductive channel will finally pass across the GB and enters the neighbor

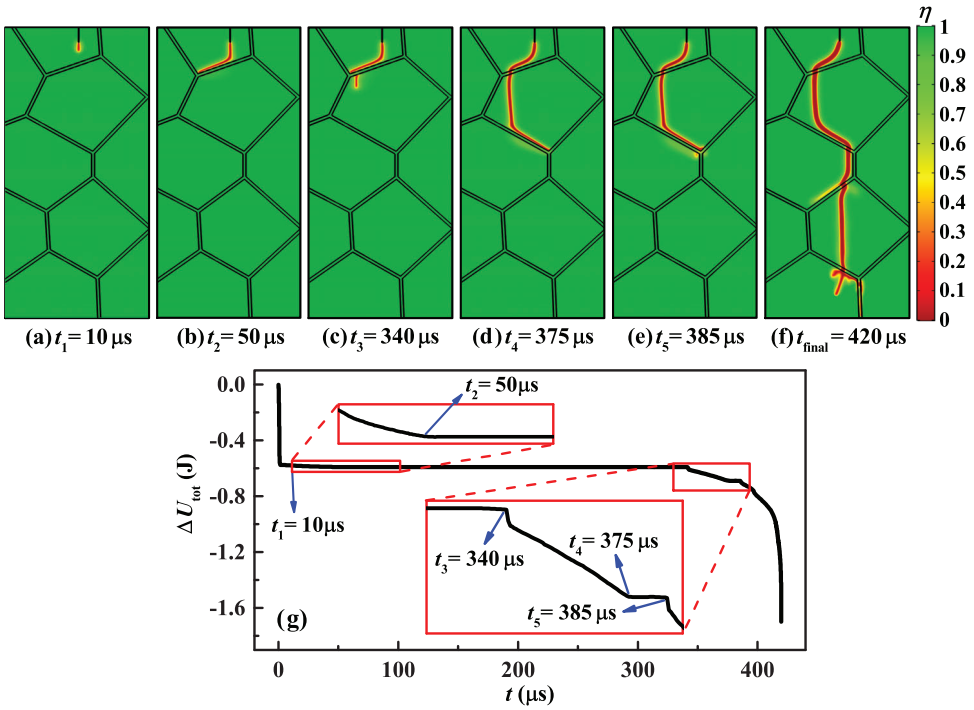

Figure 6. a–f) Contour plots of the phase field variable at different times of t_1 = 10, t_2 = 50, t_3 = 340, t_4 = 375, t_5 = 385, and t_{final} = 420 μs, respectively, and g) the time evolution of the total energy. Insets show the enlargement at the intervals 10 ≤ t ≤ 100 μs and 320 ≤ t ≤ 390 μs.

grain, and thus the total energy will be reduced (see the inset for t = 340 − 375μs). Once again, in the next GB, the total energy becomes constant, but in a very shorter time interval (see t = 375–385 μs). Finally, the complete breakdown is achieved at t = 420 μs. Note that this breakdown time is related to the threshold breakdown electric field, E_{BT}, of 108.5 kV cm^{-1} (obtained in our model). From the above results, we conclude that the dielectric breakdown is highly impacted by first grains and GBs that are usually adjacent to cavities, defects, and impurities. The dielectric breakdown strength of the cavities, defects, and impurities are much smaller than the ferroelectric material. Thus, the nucleation of the conductive channel occurs on them and propagates into adjacent grains and GBs.[47,57,60]

To check the role of grain orientation on the results, we calculated the phase field variable η for four different grain orientations, with same average grain size. The results are shown in **Figure 7**. The values of E_{BT} are indicated on the graph. As can be seen, the value E_{BT} is in the range of 108.5–112.5 kV cm^{-1}. The percent deviation from the mean value is small and less than ±2 percent. This confirms that grain orientation does not significantly affect the E_{BT}, as we expected from a polycrystalline.

As discussed above, the complete breakdown is achieved at 420 μs for threshold breakdown electric field of E_{BT} = 108.5 kV cm^{-1}. It is interesting to calculate the breakdown time, when higher electric fields are applied to the ferroelectric sample. In **Figure 8**, we presented the breakdown time for electric fields larger than 108.5 kV cm^{-1}, up to 200 kV cm^{-1}. It is seen that a small increase of E to 110.0 kV cm^{-1}, considerably decreases the time from 420 to 200 μs. Further increase in applied electric field, leads to a gradual decrease of breakdown time to few ten μs.

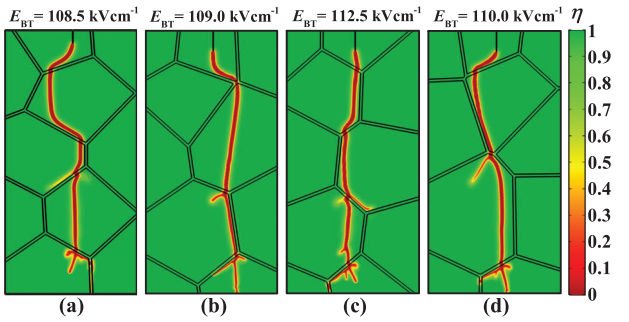

Figure 7. Contour plots of the phase field variable, for four different grain orientations. The breakdown threshold electric field strength is indicated on each case.

In order to gain further insight on the role of grain and GB parameters, we calculated E_{BT} as a function of dielectric constant of grain and GBs, that are $\varepsilon_G(0)$ and ε_{GB}, respectively, and showed the results in **Figure 9**. As it is seen, the value of E_{BT} decreases with increasing $\varepsilon_G(0)$ (Figure 9a). More importantly, for $\varepsilon_G(0) \geq 1000$, it reaches a nearly constant value. It means that for ferroelectrics with $\varepsilon_G(0) \geq 1000$, the E_{BT} is nearly independent of $\varepsilon_G(0)$. As discussed above, E_{BT} equals to 108.5 kV cm^{-1} at $\varepsilon_G(0) = 1000$ (shown by circle in Figure 9a). The role of the dielectric constant of GBs is exhibited in Figure 9b, which manifests an important result that E_{BT} increases by the decrease of ε_{GB}. The trend of E_{BT} with dielectric constant is in agreement with the experimental results, as seen for BNT-SLT ferroelectrics.[36]

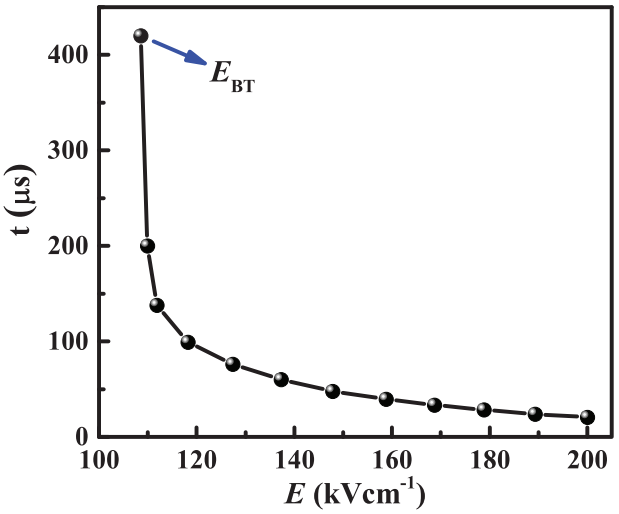

Figure 8. The dependence of breakdown time on the applied electric field. E_{BT} refers to the breakdown threshold electric field.

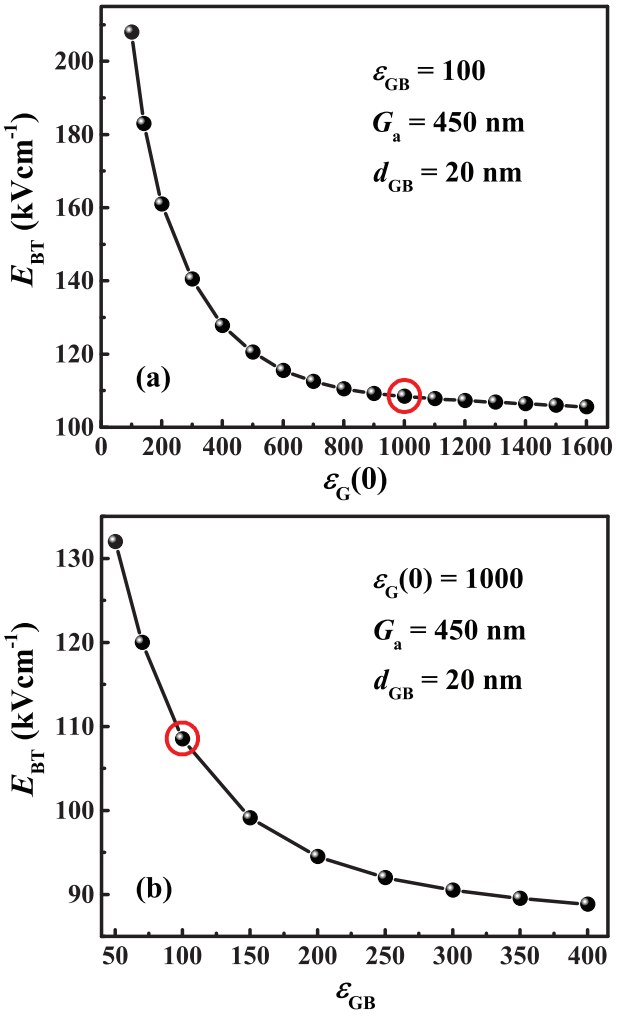

Figure 9. The breakdown threshold electric field strength, E_{BT}, as a function of a) dielectric constant of grains, $\varepsilon_G(0)$ and b) dielectric constant of GBs, ε_{GB}. The circle indicates the point obtained in the previous simulation results (Figures 5–8).

To have a complete description of the role of GBs on the breakdown phenomenon, we calculated E_{BT} as a function of GB thickness, in the range of d_{GB} = 5–40 nm. The calculated results are shown in **Figure 10**. The evolution of the phase-field variable η for three different d_{GB} of 5, 20, and 40 nm are depicted in Figure 10a–c, with corresponding E_{BT} of 71.0, 108.5, and 134.1 kV cm^{-1}, respectively. The increasing trend manifests the larger breakdown energy of GBs. The GBs act as the depletion space charge layers, which create potential barriers for the charge carriers.[61,62] The E_{BT} as function of d_{GB} could be fitted by a power function as follows (see Figure 10d)

$$E_{BT}(d_{GB}) = a(d_{GB})^n \tag{28}$$

The exponent was found to be $n = 0.2962 \pm 0.0051$.

From the above results, we can conclude that the GB parameters have a crucial impact on the ferroelectric breakdown. In this way, E_{BT} can be tuned by all the parameters, $\varepsilon_G(0)$, ε_{GB}, and d_{GB}. It means that, by engineering the GBs, one can enhance the ferroelectric parameters. These findings are in agreement with the experimental results.[63–66] In fact, advanced preparation processes such as two-step sintering,[63] grain coating by SiO_2 shell,[64,65] viscous polymer processing, and liquid-phase sintering[66] are utilized to the increase of GBs thickness, and affecting its dielectric constant.

Finally, to investigate the effect of grain size, G_a, on the value of E_{BT}, polycrystalline ferroelectric models with different G_a from 450 to 1800 nm were constructed via voronoi tessellation. The GBs thickness was fixed at d_{GB}=20 nm for all the models. The calculated results are shown in **Figure 11**. The evolution of the phase-field variable η for three grain sizes of 450, 900, and 1800 nm are depicted in Figure 11a–c, with the corresponding E_{BT} of 108.5, 79.2, and 60.1 kV cm^{-1}, respectively. It is seen that, the value of E_{BT} decreases with increase of G_a, in fact, by increasing G_a, the ratio of G_a to d_{GB} increases. Thus, GBs apply less resistance to the conductive channel propagation. As an important result, the main channel is accompanied by a number of branches. The effect of these branches is especially seen when there are cavities, defects, and impurities in the sample.[47,67] Their presence induces an avalanche propagation which results in a smaller E_{BT}. As shown in Figure 11d, the E_{BT} as function of G_a could be fitted with a power function, as follows

$$E_{BT}(G_a) = a(G_a)^{-n} \tag{29}$$

The exponent was found to be $n = 0.4271 \pm 0.0112$. This simulation result is in agreement with experimental studies. In several experimental works on $BaTiO_3$-based ferroelectrics, it has been reported that E_{BT} obeys the law $E_{BT} \propto G_a^{-n}$ with a n-value between 0.2 and 0.4.[62,68–70] As a result, by decreasing grain size to few hundred nanometers, through mechanical and/or chemical preparation processes, one can achieve enhanced breakdown strength.

4. Conclusion

In summary, a phase-field model was used to investigate the dielectric breakdown strength in a typical polycrystalline ferroelectric material. The findings show that the grains and GBs

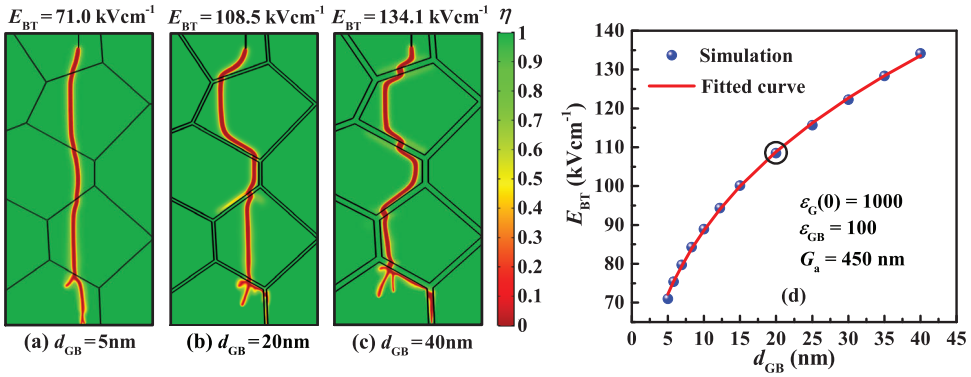

Figure 10. a–c) Contour plots of the phase field variable of the model with different d_{GB} of 5, 20, and 40 nm. The grain size is fixed at G_a = 450 nm. d) The breakdown threshold electric field strength, E_{BT}, as a function of the d_{GB}. The circle indicates the point obtained in the previous simulation results (Figures 5–8).

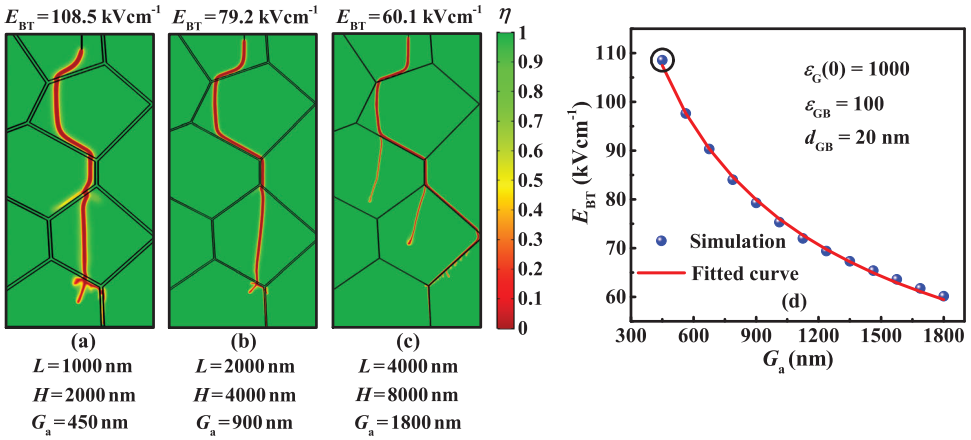

Figure 11. a–c) Contour plots of the phase field variable of the models with different L and H dimensions (equivalent to G_a of 450, 900, and 1800 nm), with a same d_{GB} of 20 nm. d) The breakdown threshold electric field strength, E_{BT}, as a function of G_a. The circle indicates the point obtained in the previous simulation results (Figures 5–8).

parameters (dielectric constant, thickness of GBs, and grain size) have a crucial impact on the dielectric breakdown. The main results are as follows: i) The threshold breakdown electric field, E_{BT}, enhances with decreasing the dielectric constant of both the grain and GBs. ii) It is found that by reducing grain size to few hundred nanometers and increasing GB thickness, a high E_{BT} can be achieved. iii) The dependence of E_{BT} on grain size (G_a) and GB's thickness (d_{GB}) obeys a power function G_a^{-n} (n = 0.42) and d_{GB}^{n} (n = 0.3), respectively. This means that by engineering grains and GBs, through modified preparation details, a high dielectric breakdown can be achieved, which is crucial to have an excellent energy storage in ferroelectric materials.

Acknowledgements

This work was supported by Iran National Science Foundation (INSF), project No. 98012941.

Conflict of Interest

The authors declare no conflict of interest.

Data Availability Statement

The data that support the findings of this study are available from the corresponding author upon reasonable request.

Keywords

breakdown electric field, grain, grain-boundaries, phase-field model, polycrystalline ferroelectric

Received: May 11, 2022
Revised: September 28, 2022
Published online: November 3, 2022

[1] Z. Yang, H. Du, L. Jin, D. Poelman, *J. Mater. Chem. A* **2021**, *9*, 18026.
[2] Z. Lu, G. Wang, W. Bao, J. Li, L. Li, A. Mostaed, H. Yang, H. Ji, D. Li, A. Feteira, F. Xu, D. C. Sinclair, D. Wang, S.-Y. Liu, I. M. Reaney, *Energy Environ. Sci.* **2020**, *13*, 2938.
[3] Y. Pu, M. Chen, X. Li, L. Zhang, F. Zhuo, W. Wang, X. Du, *J. Mater. Sci.* **2021**, *56*, 9894.
[4] S. Rukin, *Rev. Sci. Instrum.* **2020**, *91*, 011501.

[5] G. Ren, G. Ma, N. Cong, *Renewable Sustainable Energy Rev.* **2015**, *41*, 225.
[6] L. Kouchachvili, W. Yaïci, E. Entchev, *J. Power Sources* **2018**, *374*, 237.
[7] J. Piprek, *Opt. Quantum Electron.* **2019**, *51*, 60.
[8] D. Wang, T. Namihira, *Plasma Sources Sci. Technol.* **2020**, *29*, 023001.
[9] L. Yang, X. Kong, F. Li, H. Hao, Z. Cheng, H. Liu, J. F. Li, S. Zhang, *Prog. Mater. Sci.* **2019**, *102*, 72.
[10] J. Kundin, R. S. Almeida, H. Salama, H. Farhandi, K. Tushtev, K. Rezwan, *Comput. Mater. Sci.* **2020**, *185*, 109926.
[11] E. Miyoshi, T. Takaki, S. Sakane, M. Ohno, Y. Shibuta, T. Aoki, *Comput. Mater. Sci.* **2021**, *186*, 109992.
[12] Y. Rezaei, M. Jafari, M. Jamshidian, *Comput. Mater. Sci.* **2021**, *200*, 110786.
[13] R. Jeyaraam, V. S. Sarma, S. Vedantam, *Comput. Mater. Sci.* **2020**, *182*, 109787.
[14] M. Verma, R. Mukherjee, *J. Appl. Phys.* **2021**, *130*, 025305.
[15] J. Kundin, H. Farhandi, K. P. Ganesan, R. S. Almeida, K. Tushtev, K. Rezwan, *Comput. Mater. Sci.* **2021**, *190*, 110295.
[16] M. Javanbakht, M. Adaei, *J. Mater. Sci.* **2021**, *55*, 2544.
[17] M. Javanbakht, M. S. Ghaedi, E. Barchiesi, A. Ciallella, *Math. Mech. Solids* **2021**, *26*, 90.
[18] M. Javanbakht, M. Adaei, *Comput. Mater. Sci.* **2019**, *167*, 168.
[19] M. Javanbakht, M. S. Ghaedi, *Comput. Mater. Sci.* **2020**, *172*, 109339.
[20] H. Danesh, M. Javanbakht, S. Mirzakhani, *Comput. Mater. Sci.* **2021**, *194*, 110429.
[21] H. Danesh, M. Javanbakht, E. Barchiesi, N. Hamila, *Continuum Mech. Thermodyn.* **2021**.
[22] S. Kavousi, M. A. Zaeem, *Acta Mater.* **2021**, *205*, 116562.
[23] J.k. Ren, Y. Chen, Y.f. Cao, B. Xu, M.-y. Sun, D.z. Li, *J. Mater. Sci.* **2021**, *56*, 12455.
[24] C. Chen, X. Yang, *J. Comput. Phys.* **2019**, *388*, 41.
[25] F. Yu, Y. Wei, X. Liu, *Int. J. Heat Mass Transfer* **2019**, *142*, 118450.
[26] T. Takaki, S. Sakane, M. Ohno, Y. Shibuta, T. Aoki, *Comput. Mater. Sci.* **2020**, *171*, 109209.
[27] J. k. Ren, Y. Chen, B. Xu, M. y. Sun, D. z. Li, *Comput. Mater. Sci.* **2019**, *163*, 37.
[28] C. Chen, X. Yang, *J. Comput. Phys.* **2019**, *388*, 41.
[29] L. Yang, Y. Yang, H. Zheng, *Eng. Fract. Mech.* **2021**, *241*, 107427.
[30] A. Emdadi, M. A. Zaeem, *Comput. Mater. Sci.* **2021**, *186*, 110057.
[31] T. K. Mandal, V. P. Nguyen, J.-Y. Wu, *Eng. Fract. Mech.* **2019**, *217*, 106532.
[32] H. Jafarzadeh, G. H. Farrahi, M. Javanbakht, *Continuum Mech. Thermodyn.* **2020**, *32*, 913.
[33] H. Jafarzadeh, V. I. Levitas, G. H. Farrahi, M. Javanbakht, *Nanoscale* **2019**, *11*, 22243.
[34] G. H. Farrahi, M. Javanbakht, H. Jafarzadeh, *Continuum Mech. Thermodyn.* **2020**, *32*, 589.
[35] D. Zhang, X. He, X. Yang, *SIAM J. Sci. Comput.* **2021**, *43*, B167.
[36] X. Qiao, F. Zhang, D. Wu, B. Chen, X. Zhao, Z. Peng, X. Ren, P. Liang, X. Chao, Z. Yang, *Chem. Eng. J.* **2020**, *388*, 124158.
[37] W. Ma, Y. Zhu, M. A. Marwat, P. Fan, B. Xie, D. Salamon, Z. G. Ye, H. Zhang, *J. Mater. Chem. C* **2019**, *7*, 281.
[38] A. Song, J. Song, Y. Lv, L. Liang, J. Wang, L. Zhao, *Mater. Lett.* **2019**, *237*, 278.
[39] M. Zhou, R. Liang, Z. Zhou, X. Dong, *Ceram. Int.* **2019**, *45*, 3582.
[40] J. P. Silva, J. M. Silva, M. J. Oliveira, T. Weingärtner, K. C. Sekhar, M. Pereira, M. J. Gomes, *Adv. Funct. Mater.* **2019**, *29*, 1807196.
[41] H. Qi, A. Xie, A. Tian, R. Zuo, *Adv. Energy Mater.* **2020**, *10*, 1903338.
[42] P. Zhao, H. Wang, L. Wu, L. Chen, Z.Cai, L. Li, X. Wang, *Adv. Energy Mater.* **2019**, *9*, 1803048.
[43] L. F. Zhu, X. W. Lei, L. Zhao, M. I. Hussain, G. Z. Zhao, B. P. Zhang, *Ceram. Int.* **2019**, *45*, 20266.
[44] Q. Hu, Y. Tian, Q. Zhu, J. Bian, L. Jin, H. Du, D. O. Alikin, V. Y. Shur, Y. Feng, Z. Xu, X. Wei, *Nano Energy* **2020**, *67*, 104264.
[45] G. Liu, Y. Li, B. Guo, M. Tang, Q. Li, J. Dong, L. Yu, K. Yu, Y. Yan, D. Wang, L. Zhang, *Chem. Eng. J.* **2020**, *398*, 125625.
[46] Y. Li, Y. Liu, M. Tang, J. Lv, F. Chen, Q. Li, Y. Yan, F. Wu, L. Jin, G. Liu, *Chem. Eng. J.* **2021**, *419*, 129673.
[47] K. C. Pitike, W. Hong, *J. Appl. Phys.* **2014**, *115*, 044101.
[48] Z. Cai, X. Wang, W. Hong, B. Luo, Q. Zhao, L. Li, *J. Am. Ceram. Soc.* **2018**, *101*, 5487.
[49] Z. H. Shen, J. J. Wang, Y. Lin, C. W. Nan, L. Q. Chen, Y. Shen, *Adv. Mater.* **2018**, *30*, 1704380.
[50] Z. H. Shen, J. J. Wang, J. Y. Jiang, S. X. Huang, Y. H. Lin, C. W. Nan, L. Q. Chen, Y. Shen, *Nat. Commun.* **2019**, *10*, 1843.
[51] K. M. Johnson, *J. Appl. Phys.* **1962**, *33*, 2826.
[52] F. Jona, G. Shirane, *Ferroelectric Crystals*, Pergamon Press, Oxford **1962**.
[53] L. Ambrosio, V. M. Tortorelli, *Boll. Della Unione Mat. Ital.* **1992**, *6*, 105.
[54] C. Kuhn, A. Schlüter, R. Müller, *Comput. Mater. Sci.* **2015**, *108*, 374.
[55] Z. Cai, P. Feng, C. Zhu, X. Wang, *J. Eur. Ceram. Soc.* **2021**, *41*, 2533.
[56] P. Ren, Z. Liu, X. Wang, Z. Duan, Y. Wan, F. Yan, G. Zhao, *J. Alloys Compd.* **2018**, *742*, 683.
[57] L. Yang, X. Kong, Z. Cheng, S. Zhang, *J. Mater. Res.* **2021**, *36*, 1214.
[58] B. Qu, H. Du, Z. Yang, Q. Liu, T. Liu, *RSC Adv.* **2016**, *6*, 34381.
[59] P. Zhao, H. Wang, L. Wu, L. Chen, Z. Cai, L. Li, X. Wang, *Adv. Energy Mater.* **2019**, *9*, 1803048.
[60] Z. Cai, C. Zhu, H. Wang, P. Zhao, L. Chen, L. Li, X. Wang, *J. Mater. Chem. A* **2019**, *7*, 14575.
[61] R. Waser, *Ferroelectrics* **1992**, *133*, 109.
[62] L. Yang, X. Kong, F. Li, H. Hao, Z. Cheng, H. Liu, J. F. Li, S. Zhang, *Prog. Mater. Sci.* **2019**, *102*, 72.
[63] X. Wang, Y. Huan, P. Zhao, X. Liu, T. Wei, Q. Zhang, X. Wang, *J. Materiomics* **2021**, *7*, 780.
[64] P. Zhao, Z. Cai, L. Chen, L. Wu, Y. Huan, L. Guo, L. Li, H. Wang, X. Wang, *Energy Environ. Sci.* **2020**, *13*, 4882.
[65] Z. Cai, C. Zhu, H. Wang, P. Zhao, Y. Yu, L. Li, X. Wang, *J. Mater. Chem. A* **2019**, *7*, 17283.
[66] G. Liu, Y. Li, B. Guo, M. Tang, Q. Li, J. Dong, L. Yu, K. Yu, Y. Yan, D. Wang, L. Zhang, *Chem. Eng. J.* **2020**, *7*, 125625.
[67] Z. Cai, X. Wang, L. Li, W. Hong, *Extreme Mech. Lett.* **2019**, *28*, 87.
[68] T. Tunkasiri, G. Rujijanagul, *J. Mater. Sci. Lett.* **1996**, *15*, 1767.
[69] H. Y. Lee, K. H. Cho, H. D. Nam, *Ferroelectrics* **2006**, *334*, 165.
[70] B. Liu, X. Wang, R. Zhang, L. Li, *J. Am. Ceram. Soc.* **2017**, *100*, 3599.